catalysts

MDPI

Article

Cathodic Activation of Titania-Fly Ash Cenospheres for Efficient Electrochemical Hydrogen Production: A Proposed Solution to Treat Fly Ash Waste

Tariq Altalhi [1,*], Amine Mezni [1], Mohamed M. Ibrahim [1], Moamen S. Refat [1], Adil A. Gobouri [1], Ayham M. Safklou [2], Adel M. Mousli [2], Mohamed S. Attia [3], Purna K. Boruah [4,5], Manash R. Das [4,5], Jacek Ryl [6], Rabah Boukherroub [7] and Mohammed A. Amin [1,*]

1 Department of Chemistry, College of Science, Taif University, P.O. Box 11099, Taif 21944, Saudi Arabia; aminemezni@yahoo.fr (A.M.); ibrahim@tu.edu.sa (M.M.I.); moamen@tu.edu.sa (M.S.R.); a.gobouri@tu.edu.sa (A.A.G.)
2 Sustainable Environmental Works Trading Company, P.O. Box 109660, Jeddah 21351, Saudi Arabia; ayhamsaficlo@hotmail.com (A.M.S.); am666666@gmail.com (A.M.M.)
3 Chemistry Department, Faculty of Science, Ain Shams University, Abbassia, Cairo 11566, Egypt; mohamed_sam@yahoo.com
4 Advanced Materials Group, Materials Sciences and Technology Division, CSIR-North East Institute of Science and Technology, Jorhat 785006, India; pkboruah143@gmail.com (P.K.B.); mrdas@neist.res.in (M.R.D.)
5 Academy of Scientific and Innovative Research (AcSIR), Ghaziabad 201002, India
6 Institute of Nanotechnology and Materials Engineering, Faculty of Applied Physics and Mathematics, Gdansk University of Technology, Narutowicza 11/12, 80-233 Gdansk, Poland; jacek.ryl@pg.edu.pl
7 University of Lille, CNRS, Centrale Lille, Université Polytechnique Hauts-de-France, UMR 8520—IEMN, F-59000 Lille, France; rabah.boukherroub@univ-lille.fr
* Correspondence: ta.altalhi@tu.edu.sa (T.A.); mohamed@tu.edu.sa (M.A.A.)

Abstract: Fly ash (FA) is a waste product generated in huge amounts by coal-fired electric and steam-generating plants. As a result, the use of FA alone or in conjunction with other materials is an intriguing study topic worth exploring. Herein, we used FA waste in conjunction with titanium oxide (TiO_2) to create (FA-TiO_2) nanocomposites. For the first time, a cathodic polarization pre-treatment regime was applied to such nanocomposites to efficiently produce hydrogen from an alkaline solution. The FA-TiO_2 hybrid nanocomposites were prepared by a straightforward solvothermal approach in which the FA raw material was mixed with titanium precursor in dimethyl sulfoxide (DMSO) and refluxed during a given time. The obtained FA-TiO_2 hybrid nanocomposites were fully characterized using various tools and displayed a cenosphere-like shape. The synthesized materials were tested as electrocatalysts for the hydrogen evolution reaction (HER) in 0.1 M KOH solution in the dark, employing various electrochemical techniques. The as-prepared (unactivated) FA-TiO_2 exhibited a considerable HER electrocatalytic activity, with an onset potential (E_{HER}) value of −144 mV vs. RHE, a Tafel slope ($-b_c$) value of 124 mV dec^{-1} and an exchange current density (j_o) of ~0.07 mA cm^{-2}. The FA-TiO_2's HER catalytic performance was significantly enhanced upon cathodic activation (24 h of chronoamperometry measurements performed at a high cathodic potential of −1.0 V vs. RHE). The cathodically activated FA-TiO_2 recorded HER electrochemical kinetic parameters of E_{HER} = −28 mV, $-b_c$ = 115 mV dec^{-1}, j_o = 0.65 mA cm^{-2}, and an overpotential η_{10} = 125 mV to yield a current density of 10 mA cm^{-2}. Such parameters were comparable to those measured here for the commercial Pt/C under the same experimental conditions (E_{HER} = −10 mV, $-b_c$ = 113 mV dec^{-1}, j_o = 0.88 mA cm^{-2}, η_{10} = 110 mV), as well as to the most active electrocatalysts for H_2 generation from aqueous alkaline electrolytes.

Keywords: fly ash; titanium dioxide; hybrid nanocomposites; solvothermal process; hydrogen production

check for updates

Citation: Altalhi, T.; Mezni, A.; Ibrahim, M.M.; Refat, M.S.; Gobouri, A.A.; Safklou, A.M.; Mousli, A.M.; Attia, M.S.; Boruah, P.K.; Das, M.R.; et al. Cathodic Activation of Titania-Fly Ash Cenospheres for Efficient Electrochemical Hydrogen Production: A Proposed Solution to Treat Fly Ash Waste. *Catalysts* **2022**, *12*, 466. https://doi.org/10.3390/catal12050466

Academic Editor: Bruno Fabre

Received: 16 February 2022
Accepted: 12 April 2022
Published: 22 April 2022

Publisher's Note: MDPI stays neutral with regard to jurisdictional claims in published maps and institutional affiliations.

1. Introduction

Growing energy consumption, fluctuating oil costs, and environmental concerns have all contributed to the importance of renewable energy. Fuel cells, which mix hydrogen (as a fuel) and oxygen to produce heat, electricity and water, are today one of the most popular renewable energy sources [1,2], because of their remarkable efficiency and performance, cleanliness, and cost-effective power supply. Chemical energy is used in both fuel cells and batteries to produce electricity. A fuel cell never loses its charge and produces power as long as fuel is available. To function effectively, fuel cells need pure H_2 as fuel, which is commonly produced using methane reforming. This well-known commercial process, however, requires a large amount of energy (heat) to generate H_2. Furthermore, the produced H_2 is impure due to the presence of carbon dioxide (CO_2) gas as a byproduct [3–5].

The best way for producing pure H_2 electrochemically at room temperature is through water electrolysis. Efficient electrocatalysts are commended as cathode materials in water electrolysis cells, because they are able to create considerable amounts of hydrogen at low overpotentials by speeding up the kinetics of the hydrogen evolution reaction (HER) [6].

Platinum (Pt)-based materials are the most stable and efficient HER electrocatalysts. However, the exorbitant price of these components raises the overall cost of water electrolyzers. This made the development of innovative, inexpensive, and effective HER electrocatalysts one of the most important goals for large-scale H_2 production [7,8]. Electrocatalytic water splitting is also limited due to the substantial amounts of electric energy required to generate H_2 from water. Owing to its numerous advantages, such as high electron mobility, various morphologies, cheap synthesis, good photochemical stability, and lack of toxicity, titania (TiO_2) has attracted a lot of attention as a cutting-edge material in photocatalysis [9]. Recently, TiO_2 has generated a consistent interest as a material for 'dark' electrocatalysis for the production and conversion of renewable energy. The efficacy of TiO_2 as an electrocatalyst is influenced by its shape, surface area, and crystallinity, among other factors [9].

As a result, several strategies for modifying and engineering TiO_2 to boost its conductivity, and hence, catalytic activity, were employed. For example, Feng et al. [10] engineered interfacial oxygen vacancies to activate pure TiO_2 single crystals toward the HER in an alkaline solution. The experimental and theoretical findings obtained by Feng et al. revealed that the subsurface oxygen vacancies and low-coordinated Ti ions (Ti^{3+}) improved electrical conductivity and thus, facilitated electron transfer and hydrogen desorption. In another study, Swaminathan et al. [11] used an electrochemical cathodization technique to overcome the paradigm of electro-inactive titania by using defect engineering as a tool to alter the nonconductive titania's local atomic structure. Ultrafast HER kinetics are ensured by increased electro-conducting characteristics and favorable surface energetics for H_{ads} of reduced titania ($TiO_{1.23}$). TiO_2 was also combined with advanced materials, such as carbon-based materials, transitional metal dichalcogenides (TMDs), metal oxides, and metal-organic frameworks (MOFs) to boost its HER catalytic activity [9].

Electrocatalysts' cathodic polarization pre-treatment is an electrochemical technique employed to effectively enhance HER catalytic performance. This approach of cathodic activation is not only ecologically sustainable, but it also takes place in the same electrochemical cell that is employed for HER measurements thus, reducing additional costs. Despite these advantages, the literature revealed a limited number of research papers on the cathodic activation of electrocatalysts for increased catalytic activity. For instance, Prosini et al. found that cathodic polarization of a carbon nanotubes (CNTs) substrate improved its electrocatalytic activity for the HER [12]. Cui et al. [13] reported that a two-step activation process of multi-walled carbon nanotubes (MWCNTs), consisting of oxidation in HNO_3 at 120 °C for 4 h followed by 4 h of cathodic activation at −2 V vs. a saturated calomel electrode (SCE) in H_2SO_4, resulted in a significant improvement in the substrate's HER electrocatalytic activity. In another study, the HER catalytic activity of mesoporous bacterium-derived carbon electrocatalysts has been considerably enhanced upon cathodic activation in 0.1 M H_2SO_4 at −2 V vs. SCE for 4 h [14].

Some of us investigated cathodic activation of Au-Pd NPs/rGO [15], Ti-supported Au NPs [16], Au-Ni NPs/rGO [17], Au/TiO_2 [18], and hydroxyl-functionalized ZrO_2 nanoparticles [19] electrodes at high cathodic overpotentials to enhance their HER activities. Recently, we adopted a simple electrochemical activation approach to achieve good performance for the HER in an alkaline medium using a widely available and inexpensive carbon felt (CF) electrode [20].

Industrial fly ash (FA) is a hazardous by-product generated by a variety of manufacturing processes, particularly those involving significant thermal energy [21]. FA waste is released in the form of fine black dust that is easily dispersed into the atmosphere [22]. The FA appears as big, porous particles with a micrometric size of up to 25 µm [23,24]. The presence of hazardous elements, such as vanadium, cadmium, and others in FA waste induces toxicity, which has a direct impact on human and animal health and causes several environmental and ecosystem concerns [25]. Therefore, researchers all over the globe are searching for better utilization and valorization of FA waste for diverse applications [26–31]. Kunihiko et al., for example, described a mechano-chemical treatment of FA powder to produce geopolymers for environmental and materials science applications [31]. In addition, FA displays high porosity and, therefore, its large surface area can be explored for the immobilization of various nanoparticles with the aim to limit/restrict their agglomeration and enhance their catalytic/electrocatalytic activity.

In view of this, the present work deals with the utilization of FA as an effective support for TiO_2 nanoparticles immobilization to prepare an efficient hybrid catalyst for electrocatalytic hydrogen production from alkaline solutions. The objective here is to obtain the best catalytic performance feasible for the electrochemical production of H_2. For this purpose to be properly achieved, the catalyst is treated by a protracted cathodic pre-polarization (cathodic activation) at −2.0 V vs. RHE, under which H_2 gas is abundantly created.

The evolved H_2 not only strengthened the FA-TiO_2 interaction, and therefore, favored charge-transfer during the reduction of water molecules (evidenced here by EIS measurements), but also generated new active catalytic sites for H_2 generation, decreased average particle size (confirmed by HRTEM), and significantly increased the active surface area (manifested from capacitance measurements). As a result, cathodic activation of the as-prepared FA-TiO_2 catalyst greatly enhanced its HER catalytic activity approaching that of the Pt/C under otherwise similar conditions.

2. Experimental Procedure

2.1. Synthesis of FA-TiO_2 Hybrid Nanocomposites

The fly ash waste was generated at Rabigh Power Plant and handled by Sustainable Environmental works trading company. It is obtained as a residue that results from the combustion of heavy oil-fired power generators. The FA-TiO_2 nanocomposites were synthesized by adopting a simple thermal method (Scheme 1). Briefly, 5 mL of titanium butoxide precursor were mixed with 3 g of pure FA in dimethyl sulfoxide (DMSO), and the reaction mixture was then refluxed for 2 h under magnetic or mechanical stirring. The color of the reaction mixture turned black and then cooled down at room temperature. The product was collected by centrifugation and dried in an air oven at 60 °C for 12 h. After that, to crystallize the TiO_2, a thermal annealing step at 400 °C for 2 h was adopted under an inert atmosphere. The product obtained by this synthetic process was characterized by several tools to establish its morphology and composition. Bare TiO_2 NPs were prepared using the above protocol by dissolving the titanium precursor in DMSO (in the absence of FA) under refluxing conditions for 2 h.

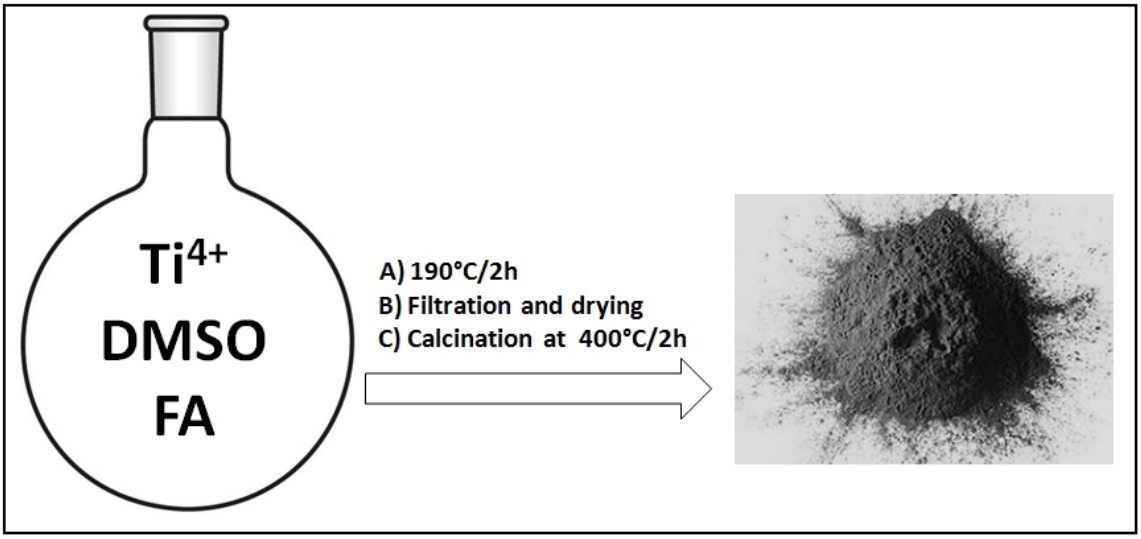

Scheme 1. Synthetic route of FA-TiO_2.

2.2. Electrochemical Measurements

Electrochemical measurements for the hydrogen evaluation reaction (HER) were carried out employing a standard double-jacketed three-electrode electrochemical cell. The cell included a graphite rod (Sigma-Aldrich, 99.999%) and a mercury/mercury oxide (Hg/HgO, NaOH (0.1 M)) as auxiliary and reference electrodes, respectively. A glassy carbon (GC, 3 mm)-loaded catalyst served as the working electrode (WE) and was prepared as described in the Supporting Information file, Section S1.

The catalytic performance of the as-prepared FA-TiO_2 nanocomposites towards the HER was investigated using linear potential sweep voltammetry. The long-term stability experiment was assessed using the cyclic voltammetry (CV) technique by applying continuous potential cycling (up to 10,000 cycles). The CV technique was also applied to calculate the electrochemical active surface area (EASA) of the as-prepared FA-TiO_2 nanocomposites. Before conducting each linear sweep voltammetry (LSV) run, the working electrode (WE) was first subjected to a prolonged cathodic activation process via applying a chronoamperometry technique for 24 h. These techniques, thoroughly described in Section S2.1 (Supporting Information), were applied to the WE/electrolyte interface via hooking up the electrochemical cell to a potentiostat, Autolab PGSTAT30/FRA system (Ecochemie, The Netherlands). The electrochemically active surface area (EASA) of the investigated catalysts was estimated using cyclic voltammetry (CV) measurements carried out at different potential sweep rates (20–120 mV s^{-1}) in the potential range (+0.1 to +0.4 V vs. RHE) that only permits the capacitive current to be recorded. The double-layer capacitance (C_{dl}) value of each tested electrocatalyst was estimated from the slope of the current density difference ($J = J_{anodic} - J_{cathodic}$) between the anodic and cathodic scans, recorded at +0.25 V vs. RHE, against the scan rate plot.

The examined electrocatalysts HER Faradaic efficiencies were measured by dividing the amount of H_2 released during 1 h of controlled galvanostatic electrolysis by the predicted volume of H_2 computed theoretically during that electrolysis, as fully described in Section S2.3 (Supporting Information).

The reproducibility of results was verified by repeating each run at least three times. The resulting data were found to be statistically respectable. The arithmetical mean and standard deviation were determined and registered for each reported value.

3. Results and Discussion

3.1. Structural and Morphological Features of FA-TiO_2 Nanocomposite

The structure and phase crystallinity of the FA-TiO_2 were examined by X-ray diffraction (XRD) analysis. Figure 1 illustrates the diffractograms of bare TiO_2 nanoparticles and the prepared hybrid FA-TiO_2 nanocomposite. All the observed diffraction planes belong to TiO_2 with the anatase structure phase (JCPDS21-1276). Its characteristic (101) diffraction peak appears clearly at $2\theta = 25.5^{\circ}$. Meanwhile, no other peaks were detected, suggesting the high purity of the as-synthesized FA-TiO_2 cenospheres. Compared to pure TiO_2 NPs, the XRD plot of the FA-TiO_2 exhibits a similar pattern, and all TiO_2 characteristic peaks can be also detected and indexed with no change concerning the position of diffraction peaks. The results from the XRD analysis showed that the incorporation of TiO_2 into FA waste had no effects on the crystal structure of the TiO_2 NPs.

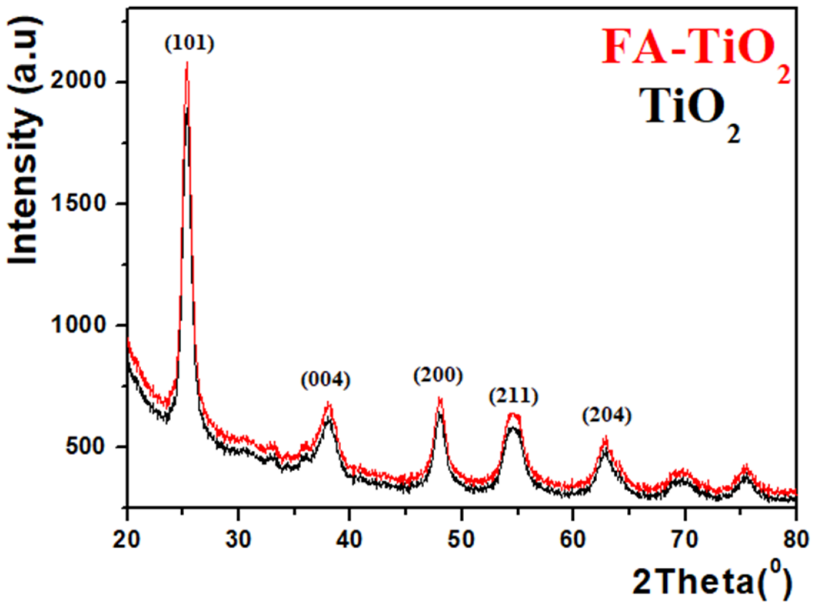

Figure 1. XRD patterns of TiO_2 NPs and FA-TiO_2 nanocomposite prepared using the solvothermal process.

Figure 2 depicts the typical scanning electron microscopy (SEM) images of FA and FA-TiO_2 cenospheres taken at different magnifications. The cenospheres exhibit a spherical shape with sizes varying between ~10 and 100 μm. The average diameter of the as-synthesized FA-TiO_2 cenospheres was approximately 70 μm, as estimated from the SEM images. It could be seen that the original FA cenospheres had a smooth surface (Figure 2a–c). The overall morphology of the cenospheres did not change after hybridization with TiO_2. Nevertheless, it can be seen in Figure 2 that the compactness of the modified FA cenospheres with TiO_2 was improved. However, the SEM image of the FA-TiO_2 cenospheres revealed that the majority of FA pores were filled by TiO_2 NPs, suggesting the successful incorporation of TiO_2 into the FA (Figure 2d–f).

It was clearly observed from the TEM and HRTEM images (Figure 3) that some aggregated TiO_2 NPs with nanometer size were distributed on the cenospheres' surface. It was noticed that a highly ordered particulate layer of TiO_2 was formed on the surface of the FA cenospheres. Analyzing the high-resolution image displayed in Figure 3, lattice fringes could be evidently distinguished as 0.352 nm, which can be attributed to the (101) lattice planes of anatase TiO_2. The EDX spectrum of the hybrid FA-TiO_2 cenospheres (Figure 4) revealed the presence of oxygen, vanadium, magnesium, molybdenum, and sulfur elements in the FA original sample, whereas additional titanium element was detected in the EDX spectrum of the hybrid FA-TiO_2 cenospheres.

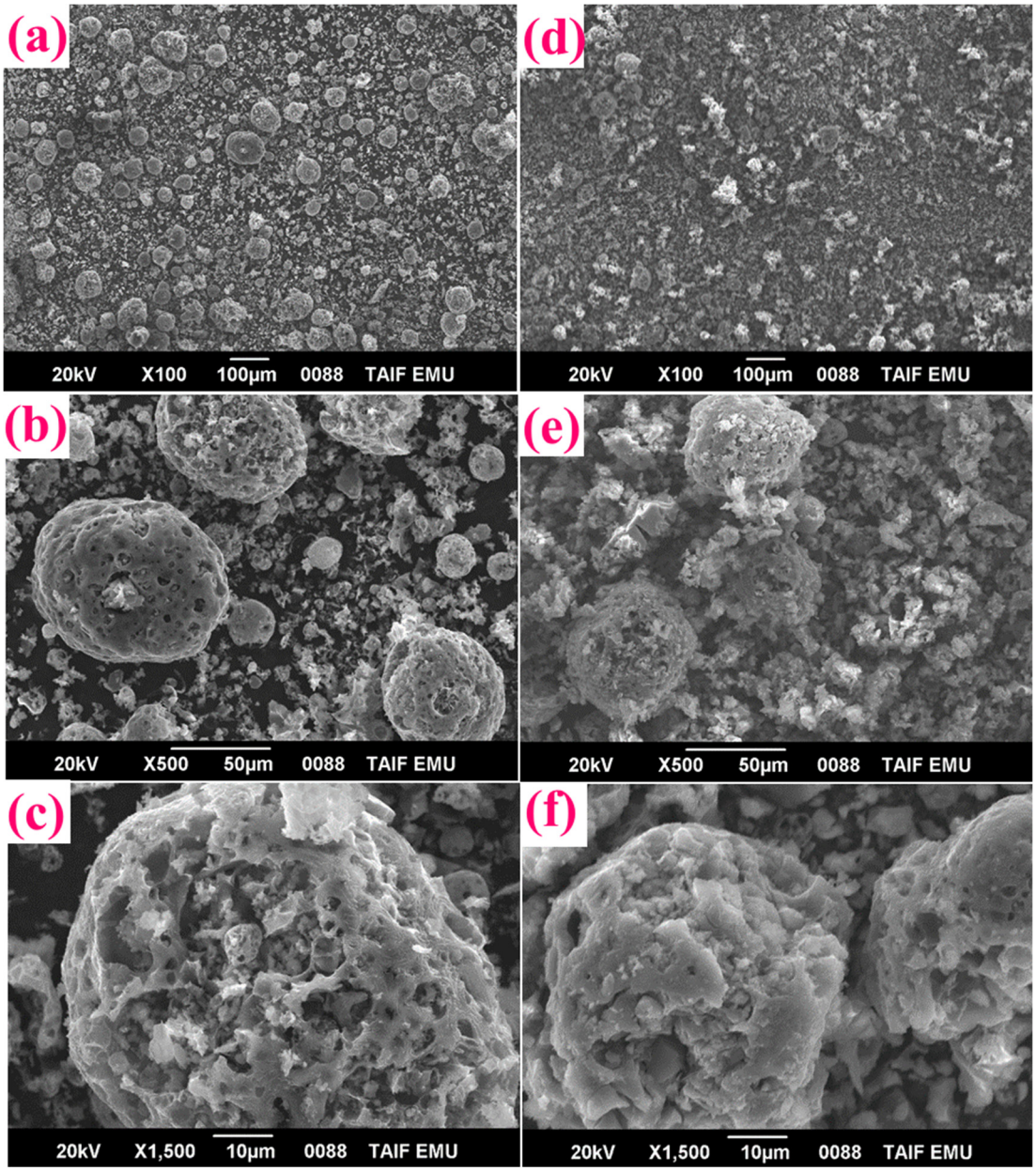

Figure 2. SEM micrographs of the outer surface of (**a**–**c**) original FA and (**d**–**f**) FA-TiO_2 cenospheres, taken at different magnifications.

Figure 5 depicts the TGA and DTA curves of the initial FA cenospheres before and after hybridization with TiO_2 NPs. A narrow exothermic peak in the range of 400–600 °C accompanied by a big weight loss was evident in both plots. Based on the literature data [18], this could be assigned to the desorption of chemisorbed OH groups. Furthermore, it can be observed that, in the case of pure FA cenospheres, the decomposition started at 420 °C whereas the FA-TiO_2 cenospheres started to decompose at 550 °C. The difference in TGA decomposition temperature may be caused by the protective effect of TiO_2. The thermal analysis experiments further indicated the change in the morphology/composition of the original FA after the incorporation of TiO_2 NPs. The thermogravimetric analysis evidenced that the hybrid FA-TiO_2 is more stable due to the protective effect induced by TiO_2 NPs.

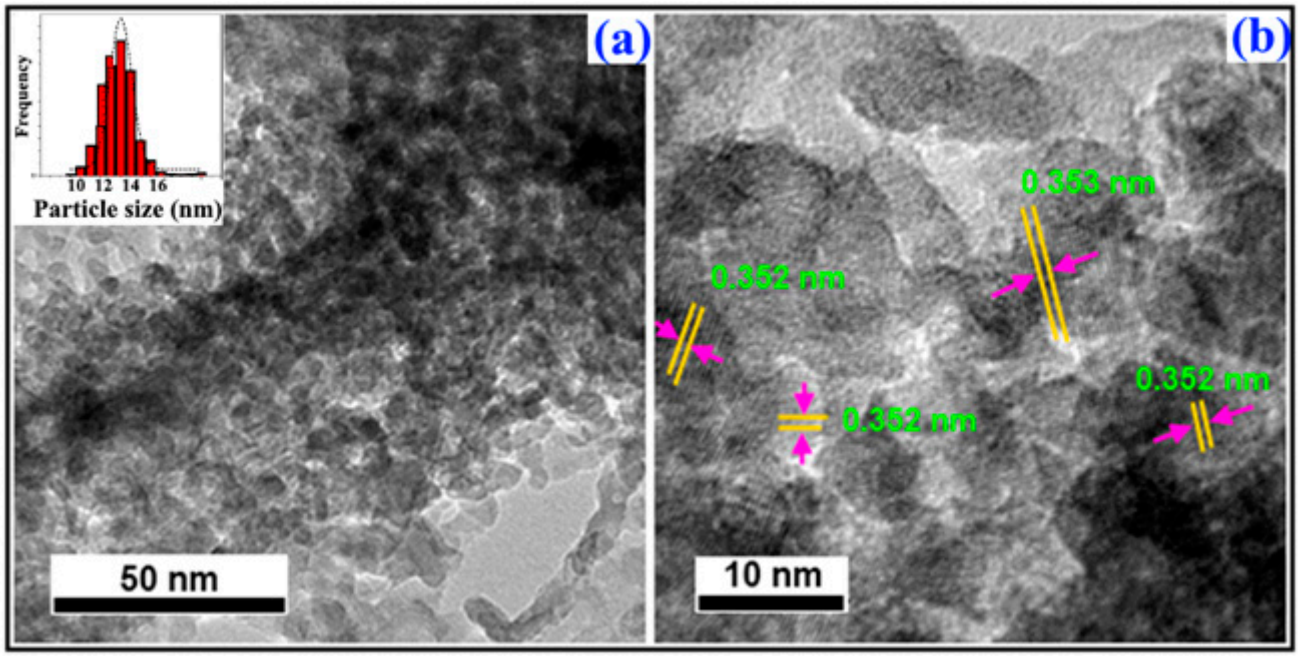

Figure 3. TEM (**a**) and HRTEM (**b**) images of TiO_2 nanoparticles coated FA cenospheres. The inset presents the particle size distribution of the nanomaterials.

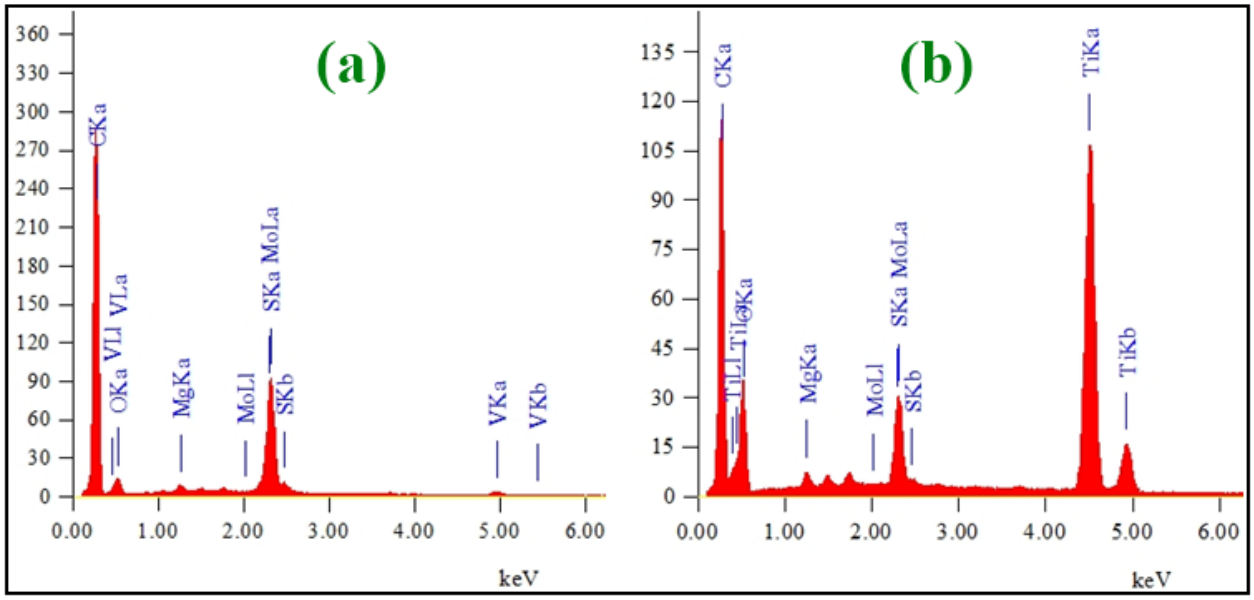

Figure 4. EDX spectra of (**a**) original FA and (**b**) FA-TiO_2 nanocomposite.

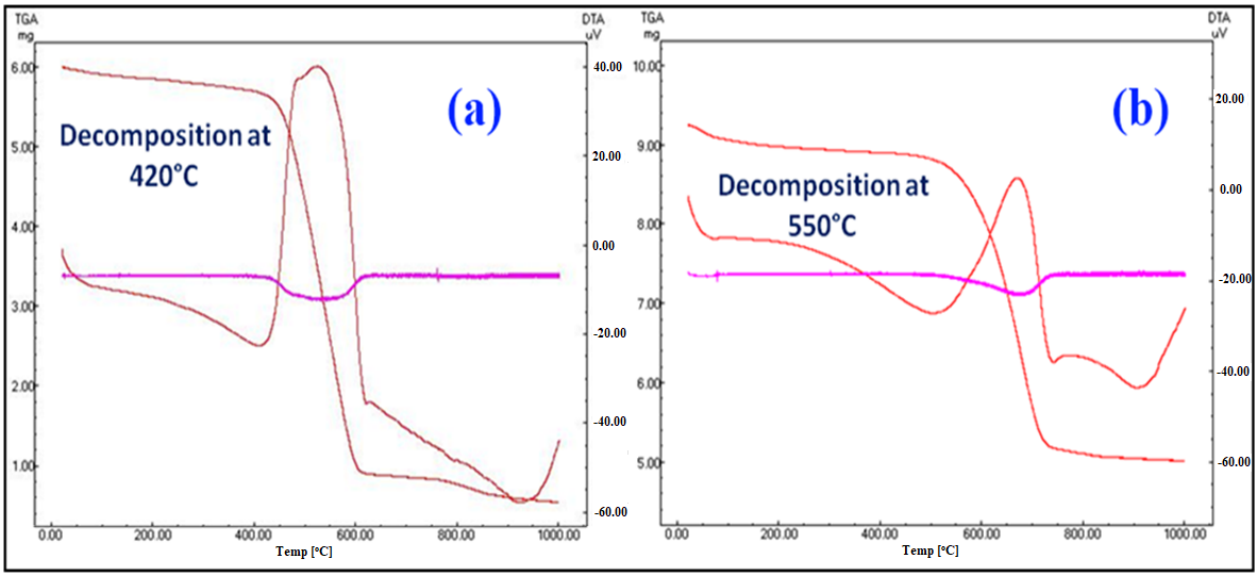

Figure 5. TGA/DTA curves of (**a**) original FA and (**b**) FA-TiO_2 recorded from room temperature to 1000 °C.

X-ray photoelectron spectroscopy (XPS) was used to examine the chemical composition and bonding of the hybrid FA-TiO_2 nanocomposite. Figure 6 displays the high-resolution XPS spectra carried out for FA, bare TiO_2, and FA-TiO_2 nanocomposite.

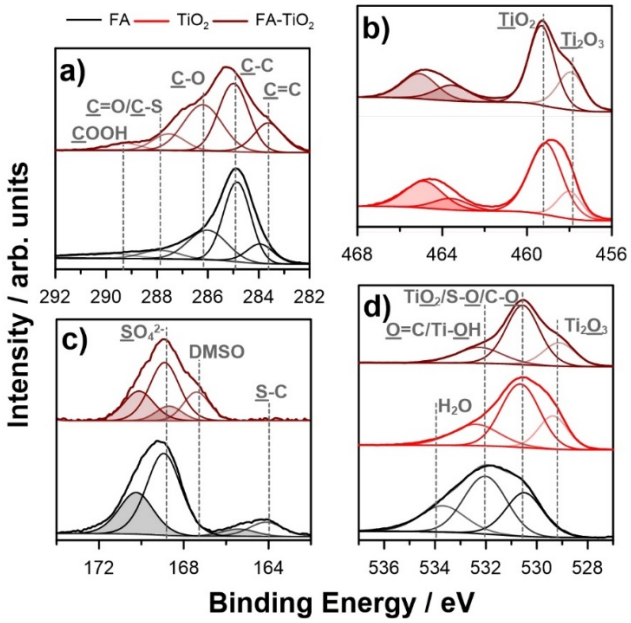

Figure 6. High-resolution XPS spectra in the core binding energy level of C 1s (**a**), Ti 2p (**b**), S 2p (**c**) and O 1s (**d**) for FA (**a**,**c**,**d**), bare TiO_2 (**b**,**d**) and FA-TiO_2 nanocomposite (**a**–**d**).

The C 1s spectrum (Figure 6a) of the FA sample reveals a complex nature, with multiple chemical states. The primary component is observed at 284.8 eV, which is characteristic of aliphatic carbon-sp^3 (C–C), and graphitic carbon-sp^2 (C=C) at 283.8 eV [32,33]. These two species represent 37 at.% of all FA constituents. The next three peaks, present in the core energy levels, are typical for oxidized carbon bonds as C–O (285.9 eV), C=O (287.8 eV) and O=C–O (289.3 eV) [32,34,35]. A similar analysis carried out for the FA-TiO_2 composite revealed a significant decrease in the total share of all carbon forms. Notably, the FA-TiO_2 synthesis has led to the relative increase of C–O bonded species. The C–O/C–C ratio rises

from 0.52 for FA to 0.85 for FA-TiO_2, which might be the sign of C–O–Ti bond formation between TiO_2 and FA within the nanocomposite. Table 1 summarizes all observed peaks with their binding energy positions and surface chemical composition (in at.%).

Table 1. The surface chemical composition (at.%) deduced from the high-resolution XPS spectra deconvolution of bare TiO_2 and FA-TiO_2 nanocomposite.

	Ti $2p_{3/2}$		**C 1s**					**O 1s**				**S $2p_{3/2}$**		
	TiO_2	**Ti_2O_3**	**C=C**	**C–C**	**C–O**	**C=O/C–S**	**COOH**	**TiO_2/S–O/C=O**	**Ti_2O_3**	**C–O/Ti–OH**	**H_2O**	**SO_4^{2-}**	**DMSO**	**S–C**
BE/eV	459.1	457.8	283.8	284.8	285.9	287.8	289.3	530.5	529.2	532.1	533.9	168.9	167.2	164.0
FA	–	–	7.6	30.3	16.0	4.6	3.9	10.3	–	15.2	7.6	3.8	–	0.7
TiO_2	24.9	7.0	–	–	–	–	–	48.5	10.6	9.0	–	–	–	–
FA-TiO_2	13.5	6.7	2.7	6.3	5.4	1.6	0.7	29.1	11.0	21.1	–	1.3	0.6	–

The deconvoluted Ti 2p spectrum (Figure 6b) suggests a dominant presence of the Ti $2p_{3/2}$ component at 459.1 eV, which is characteristic of TiO_2 NPs [16,18,36]. The binding energy of a second, weaker component at 457.8 eV is attributed to Ti_2O_3 species in the FA-TiO_2 nanocomposite. The TiO_2 share in the reference sample, based on the total Ti signal, is 78% (Table 1). On the other hand, the Ti $2p_{3/2}$ of FA-TiO_2 nanocomposite exhibits an increased amount of Ti_2O_3 species, by half, up to 33%. The formation of C-O bonds between FA and TiO_2 facilitates TiO_2 reduction and the formation of Ti_2O_3.

As testified by the EDX analyses, the FA contains some amount of sulfur, which, similar to other studies on FA, was primarily in the form of sulfates, as seen by the peak doublet with S $2p_{3/2}$ at 168.9 eV (Figure 6c) [36,37]. The same peak was distinguished for the FA-TiO_2 nanocomposite, next to a slightly weaker component derived from DMSO and located at slightly lower binding energies [38].

The high-resolution spectra of the O 1s of FA, TiO_2 and FA-TiO_2 samples are presented in Figure 6d. The binding energy at 530.5 eV of the TiO_2 evidenced the characteristic stoichiometric titanium (IV) oxides and the binding energy at 532.1 eV corresponds to surface hydroxyl groups and non-lattice oxygen [18,39,40]. The third, weaker component at lower core energy level could be ascribed to Ti_2O_3 based on the literature data and Ti:O stoichiometry. On the other hand, the primary O 1s signal for the FA sample was deconvoluted into two components at 532.1 and 530.5 eV corresponding to C=O species and sulfates and oxidized carbon (C–O) present in the fly ash, respectively. Thus, it should be noted that for FA-TiO_2 nanocomposites the O 1s spectrum is built of multiple components with peaks overlapping at characteristic binding energies. Finally, the O 1s spectrum exhibits a peak at a binding energy of 533.9 eV ascribed to chemisorbed water and disappeared upon the high-temperature treatment during FA-TiO_2 synthesis. When analyzing the O 1s spectrum recorded for the FA-TiO_2 nanocomposite, one can confirm previously drawn conclusions on the appearance of C–O–Ti bonds, based on the 531.2 eV signal strength (15.2% for FA, 9.0% for TiO_2, 21.1% for FA-TiO_2), together with TiO_2 reduction to Ti_2O_3.

Based on these results, we can conclude that the TiO_2 NPs are strongly attached to FA. This result is in good agreement with DTA/TGA measurements. However, the decomposition of pure FA starts at 420 °C, while the decomposition of FA-TiO_2 nanocomposite starts at 550 °C (Figure 5). Indeed, in the FA-TiO_2 nanocomposite, more energy is required to break both intrinsic bonds of FA and the extrinsic bonds of attached TiO_2 NPs. This strong affinity of FA with TiO_2 makes both materials more efficient in an electrocatalytic application, which is expected to facilitate the charge transfer between the two materials.

3.2. Electrochemical Measurements

3.2.1. Chronoamperometry Measurements (Catalyst Cathodic Activation)

The as-prepared catalysts, namely GC-FA, GC-TiO_2 and GC-(FA-TiO_2) electrodes, including the bare GC support, were subjected to a prolonged cathodic activation process (24 h of chronoamperometry measurements at a cathodic potential of −1.0 V vs. RHE) before conducting cathodic polarization measurements, as shown in Figure 7.

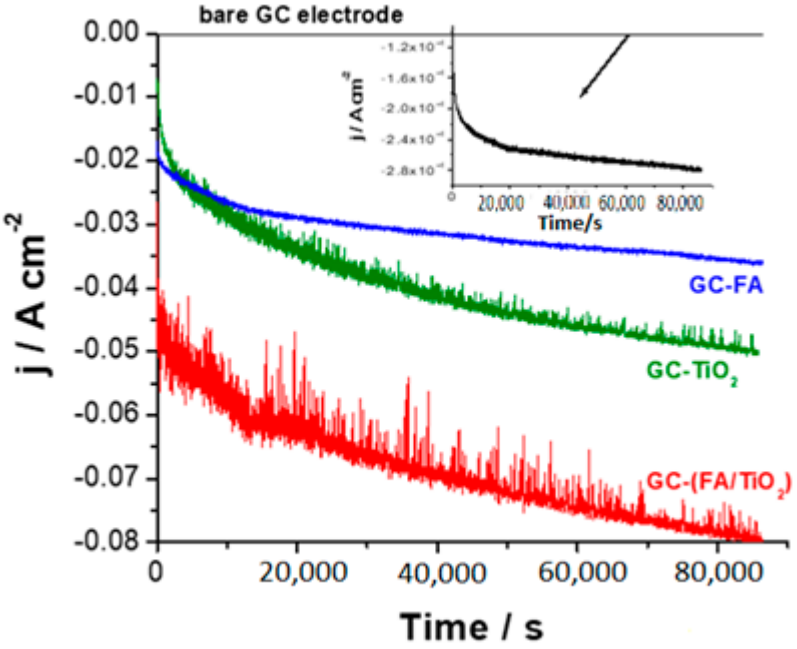

Figure 7. 24 h of Chronoamperometry measurements recorded for the investigated catalysts in deaerated 0.1 M KOH solution at −1.0 V (vs. RHE) at room temperature. Inset—the arrow refers to a zoomed chronoamperometry curve recorded for the bare GC electrode.

The current spikes, which obviously enhance going from GC-FA to GC-(FA-TiO_2), indicate a persistent rivalry between H_2 bubbles liberation and piling up processes. Despite such a continued competition between H_2 bubble release and accumulation processes, the net effect is a rise in the cathodic current throughout the run, indicating catalyst activation. The aggregation of bubbles during H_2 piling up is thought to disconnect the catalyst's active sites in the electrolyte from the electroactive species thus, impeding charge transfer and lowering current (catalyst deactivation). The current is then boosted by the release of gas (catalyst reactivation), freeing up the active sites for another H_2O molecule reduction process [15–20].

It is worth noting that the increase in cathodic current occurs to an extent depending upon the type of the tested catalyst. The bare GC electrode exhibited similar behavior, but with inferior currents, as depicted in the inset of Figure 7. This large difference in current between the substrate (the bare GCE) and the catalyst loaded on GCE is most probably caused by the catalytic impact of the supported active material. The increased cathodic current refers to the catalytic impact of H_2 gas profusely evolved during cathodic activation. The role of the cathodic activation process in enhancing HER kinetics over FA-TiO_2 catalyst will be discussed in detail later on.

At any given time during catalyst activation, the current enhancement follows the sequence: GC-FA < GC-TiO_2 < GC-(FA-TiO_2). These results highlight the higher HER catalytic activity of GC-(FA-TiO_2) catalyst compared to FA and TiO_2 taken separately. These findings suggest that the HER kinetics on FA-TiO_2 profits from FA and TiO_2 nanoparticles' cohabitation, most likely through a cooperative (synergistic) relationship.

3.2.2. Cathodic Polarization Measurements

Figure 8a displays the cathodic polarization curves of the investigated catalysts before and after cathodic activation. Measurements were conducted in 0.1 M KOH solutions at room temperature, and curves were cathodically swept at a scan rate of 5.0 mV s^{-1} starting from the corrosion potential (E_{corr}) up to a cathodic potential of 1.5 V vs. RHE. Table 2 depicts the various HER electrochemical kinetic parameters associated with these measurements. These parameters, conventionally used to assess the efficiency of the catalytic reaction, were derived from the corresponding Tafel lines, Figure 8b, constructed via fitting the experimental polarization data, Figure 8a, with the Tafel equation, Equation (1):

$$\eta_{H2/2H+} = \beta_c \log j + a \quad (1)$$

where η represents the overpotential, which is the difference between the electrode and standard potentials ($\eta = E - E_o$), j denotes the current density, β_c (the cathodic Tafel slope) = $(2.3RT/\alpha F)$ and $a = (2.3RT/\alpha F) \log j_o$, with α being the transfer coefficient, F the Faraday's constant, R the universal gas constant, T the absolute temperature, and j_o is the exchange current density.

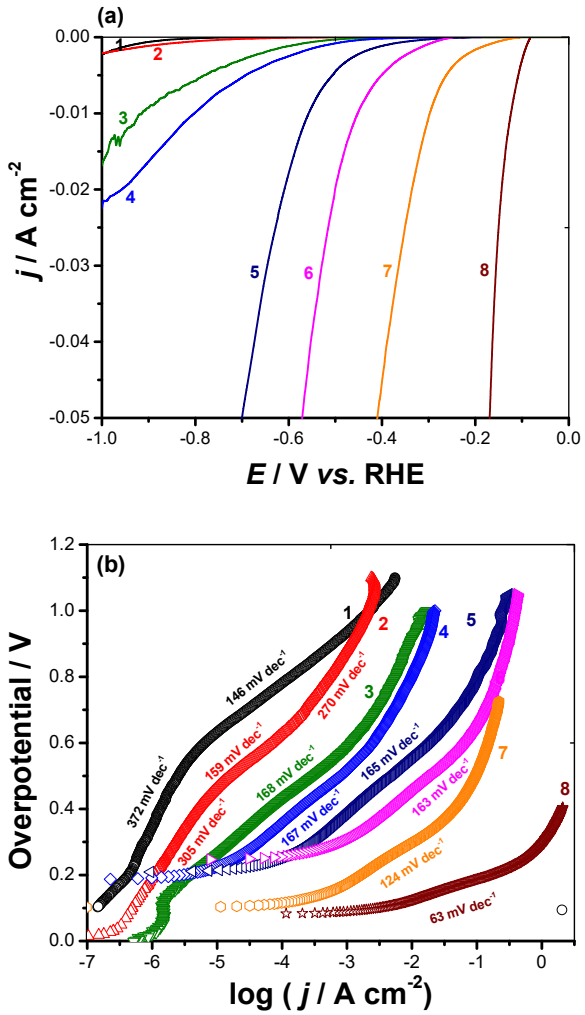

Figure 8. Linear cathodic polarization curves (**a**) and the corresponding Tafel plots (**b**) recorded for the investigated catalysts. Measurements were conducted in deaerated 0.1 M KOH solution at a scan rate of 5.0 mV s^{-1} at room temperature.(1) bare GC electrode (unactivated); (2) bare GC electrode (activated); (3) GC-FA (unactivated); (4) GC-FA (activated); (5) GC-TiO_2 (unactivated); (6) GC-TiO_2 (activated); (7) GC-(FA-TiO_2) (unactivated); (8) GC-(FA-TiO_2) (activated).

Table 2. Mean value (standard deviation) of the electrochemical HER kinetic parameters on the tested electrocatalysts (unactivated and cathodically activated). Measurements were conducted at room temperature in deaerated 0.1 M KOH solution.

Tested Cathode	Onset Potential (E_{HER})/mV vs. RHE)	Tafel Slope ($-\beta_c$, mV dec^{-1})	Exchange Current Density (j_o, mA cm^{-2})	Cathodic Potential at j = 10 mA cm^{-2} (η_{10}, mV vs. RHE)
bare GC (unactivated)	−886 (10.4)	—	—	—
bare GC (activated)	−793 (9.2)	—	—	—
GC-FA (unactivated)	−534 (6.0)	168 (1.9)	2.14 (0.04) × 10^{-4}	737 (8)
GC-FA (activated)	−468 (5.2)	167 (2.1)	5.9 (0.1) × 10^{-4}	677 (7.4)
GC-TiO_2 (unactivated)	−338 (3.8)	165 (1.8)	4.0 (0.07) × 10^{-3}	554 (6.2)
GC-TiO_2 (activated)	−282 (3.1)	163 (1.7)	1.8 (0.04) × 10^{-2}	443 (5.0)
GC-(FA-TiO_2) (unactivated)	−144 (1.8)	124 (1.7)	6.8 (0.1) × 10^{-2}	160 (3.3)
GC-(FA-TiO_2) (activated)	−28 (0.5)	115 (1.4)	65 (1.3) × 10^{-2}	125 (1.6)
Pt/C	10 (0.2)	113 (1.2)	88 (1.2) × 10^{-2}	110 (1.4)

It follows from Figure 8a that the bare GC cathodes (both unactivated, curve 1 and activated, curve 2) show inferior catalytic activity with highly negative onset potential values (E_{HER}) for the HER (−886 and −793 mV vs. RHE for the unactivated and cathodically activated GC electrodes, respectively), and very low cathodic currents. The other studied catalysts (unactivated and activated), curves 3–8, exhibited catalytic activity far beyond that of the bare GC electrode. The E_{HER} values of the activated catalysts (curves with even numbers) are smaller (more anodic) and their cathodic polarization curves become steeper (i.e., large cathodic currents can be generated at low overpotentials, corresponding to faster HER kinetics) than the corresponding unactivated ones (curves with the odd numbers). The promising HER catalytic activity of the cathodically activated GC-(FA-TiO_2) catalyst (curve 8) is evidenced by its close proximity to the HER catalytic performance of the most active non-precious electrocatalysts reported in the literature (Table S1, Supporting Information), corresponding to faster HER kinetics. For any tested catalyst (unactivated and activated), the E_{HER} value is always smaller and the cathodic current is larger for the FA-TiO_2 catalyst than FA alone and TiO_2 alone, confirming synergism between FA and TiO_2.

The overpotentials at a cathodic current density of 10 mA cm^{-2} (η_{10}), one of the most essential parameters that control the electrocatalysts' HER activity (the lower the η_{10} value the higher is the catalyst's HER performance [41]), were also compared, Table 2. The lowest η_{10} value was recorded for the cathodically activated catalysts. For instance, the η_{10} value (120 mV) achieved for the activated FA-TiO_2 catalyst to deliver a current density of 10 mA cm^{-2} is 40 mV more anodic than that measured for the unactivated one (160 mV).

The reduced E_{HER} and η_{10} values of the activated catalysts resulted in higher exchange current densities, j_o, corresponding to accelerated HER kinetics. The cathodically activated FA-TiO_2 catalyst recorded the highest j_o value (0.11 mA cm^{-2}) among the studied catalysts, which is 3.0 times greater than its j_o value (0.036 mA cm^{-2}) before activation. These findings again highlight the obvious catalytic impact of the cathodic activation process.

The Tafel slope is a useful metric for evaluating catalysts' effectiveness while simultaneously offering a valuable measure of the mechanistic processes of HER reaction [42,43]. In alkaline electrolytes, based on the classical theory, the evolution of hydrogen occurs through three main reaction steps [41]:

$$H_2O + e^- + S^* \rightarrow H_{ads} + OH^- \quad \text{(Volmer step)} \qquad (2)$$

$$H_2O + e^- + H_{ads} \rightarrow H_2 + OH^- + S^* \quad \text{(Heyrovsky)} \tag{3}$$

$$H_{ads} + H_{ads} \rightarrow H_2 + S^* + S^* \quad \text{(Tafel step)} \tag{4}$$

where S^* symbolizes the catalyst surface's active adsorption site. Two primary pathways are usually suggested for the HER, namely the Volmer-Heyrovsky reaction, Equations (2) and (3), and the Volmer-Tafel reaction, Equations (2) and (4) [44,45]. The Tafel slope value of 63 mVdec^{-1} recorded for the cathodically activated GC-(FA-TiO_2) catalyst in the current study indicates that the HER is most likely dominated by both the electron reduction of the hydronium ions (H_3O^+), which supplies an active adsorbed hydrogen atom (H_{ads}), Equation (2), and electrochemical hydrogen desorption, Equation (3), (Volmer-Heyrovsky mechanism).

The high Tafel slope value (124 mV dec^{-1}), estimated for the GC-(FA-TiO_2) catalyst before activation suggests the Volmer step, Equation (2), as the main reaction step controlling the HER. The HER kinetics for the non-activated catalyst are constrained by the inefficient number of the catalytically active sites where the adsorption of the water molecule occurs, as inferred by its large Tafel slope (124 mV dec^{-1}) [46]. On the other hand, the reduced Tafel slope of the cathodically activated catalyst (63 mV dec^{-1}) indicates that the number of attainable active sites on the catalyst surface has increased upon cathodic activation [12–20].

The electrochemical active surface area (EASA), which is directly related to the kinetics of the HER over electrocatalysts, is another significant metric for comparing the catalytic performance of different electrocatalysts. EASA is also intimately associated with the electric double-layer capacitance (C_{dl}) [47–49]. As a result, C_{dl} is utilized to determine the value of EASA. The C_{dl} values were calculated employing cyclic voltammetry (CV) measurements performed within the non-faradic potential zone. CV measurements were conducted as a function of the potential scan rate (ca. 20–120 mV s^{-1}) for each tested electrocatalyst. Figure 9a represents the comparative CV curves of the studied electrocatalysts performed at a potential sweep rate of 100 mV s^{-1}.

The values of C_{dl} (Table 3) were determined from the slopes of the current density against potential scan rate plots (Figure 9b). From Table 3, C_{dl} values of 3.9, 9.4, and 23.7 mF cm^{-2} were recorded for GC-FA, GC-TiO_2, and GC-(FA-TiO_2), respectively. Subjecting these electrocatalysts to 24 h of cathodic activation resulted in an apparent increase in their C_{dl} values to 6.6, 17.8, and 39.7 mF cm^{-2} for GC-FA, GC-TiO_2, and GC-(FA-TiO_2), respectively. These findings affirm the catalytic influence of the supporting material (TiO_2) and the cathodic polarization pre-treatments on the HER kinetics, as electrocatalysts with larger C_{dl} values possess affluence of attainable active surface sites [47–49]. This, in turn, facilitates charge transfer, leading to improved HER catalytic performance.

Table 3. Double-layer capacitance (C_{dl}), electrochemical active surface area (EASA), net voltammetry charge (Q), and the number of active sites (n) estimated for the investigated electrocatalysts from CV measurements.

Tested Cathode	C_{dl}/mF cm^{-2}	EASA/cm^2	$Q_{net} \times 10^3$/C @100 mV s^{-1}	$n \times 10^8$/mol
GC-FA (unactivated)	3.9	130	9.4	4.87
GC-FA (activated)	6.6	220	21.2	10.99
GC-TiO_2 (unactivated)	9.4	313	24.9	12.9
GC-TiO_2 (activated)	17.8	593	28.5	14.77
GC-(FA-TiO_2) (unactivated)	23.7	790	33.9	17.58
GC-(FA-TiO_2) (activated)	39.7	1323	96.8	50.16

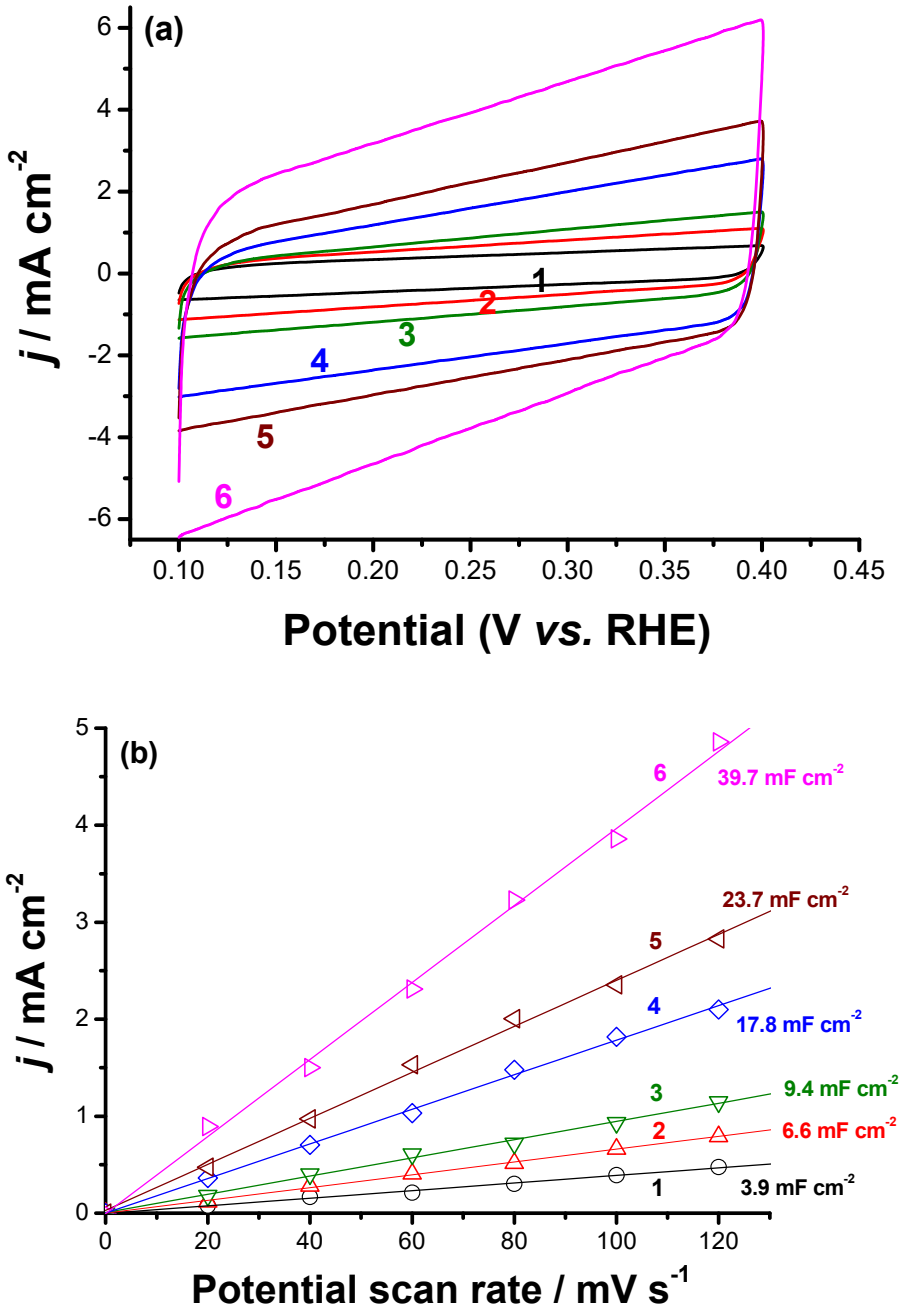

Figure 9. (**a**) CV measurements recorded for the investigated electrocatalysts. Measurements were conducted in 0.1 M KOH aqueous solution at a scan rate of 100 mV s^{-1} at room temperature. (**b**) Double-layer capacitance measurements for determining the catalyst's electrochemically-active surface area: (1) GC-FA (unactivated); (2) GC-FA (activated); (3) GC-TiO_2 (unactivated); (4) GC-TiO_2 (activated); (5) GC-(FA-TiO_2) (unactivated); (6) GC-(FA-TiO_2) (activated).

The apparent increase in the C_{dl} values after cathodic activation results from the increased EASA values of the cathodically activated samples, as shown in Table 3. However, there is a considerable improvement in cathodic current density among the investigated cathodically activated samples, as presented in Figure 9. Thus, the high HER catalytic activity of the cathodically activated samples is not just due to the change in active surface area, but also due to the structural changes that occurred at the atomic level due to the cathodic polarization pre-treatments.

The value of EASA is obtained by dividing the C_{dl} value by C_s, Equation (5), Table 3 [50].

$$EASA = C_{dl}/C_s \quad (5)$$

where C_s is the specific capacitance of a flat electrode with a surface area value of 1.0 cm^2, typically between 20 and 40 μF cm^{-2} [50]. An average C_s value of 30 μF cm^{-2} was applied in this study. The EASA values in Table 3 are obtained by substituting this C_s value in Equation (5). It is observed that the value of EASA rises upon loading FA on TiO_2. The EASA value is found to be increased with cathodic activation for all tested samples.

To acquire a better understanding of the cathodically activated samples' high intrinsic HER catalytic activity, the number of active sites n was estimated using Equation (6) [47]:

$$n = Q_{net}/2F \quad (6)$$

where Q_{net} is the net voltammetry charge of the catalyst, as determined by CV measurements. The charges generated by the bare GC electrode are subtracted from the charges produced by the investigated catalyst to estimate Q_{net} ($Q_{net} = Q_{GC\text{-}catalyst} - Q_{bare\ GC}$). The number 2 denotes the number of electrons consumed in the HER reaction, whereas F corresponds to the Faraday constant (96,485 C/mol). Table 3 also depicts the values of Q and n recorded for the studied electrocatalysts (unactivated and activated). The considerable rise in the value of n produced by the cathodic polarization pre-treatments (cathodic activation) performed on FA and FA-TiO_2 nanocomposite suggests increased catalytic activity. The cathodically activated FA-TiO_2 electrocatalyst has the greatest n value (50.16 × 10^{-8} per mol), confirming its exceptional HER catalytic activity. As shown in Table S1, the high HER catalytic performance of the cathodically activated FA-TiO_2 electrocatalyst outperformed those of active electrocatalysts previously reported in the literature (Supporting Information).

The formula shown in Equation (7) is used to compute the per-site turnover frequencies (TOFs, s^{-1}).

$$TOF = |I|/2Fn \quad (7)$$

where I refers to the cathodic (catalytic) current value (expressed in A cm^{-2}) measured at a particular overpotential. Equation (8) is obtained by combining Equations (6) and (7):

$$TOF = |I|/Q \quad (8)$$

Based on Equation (8), the current densities acquired from LSV measurements, Figure 7, can be converted to TOF values, as shown in Figure 9. It follows from Figure 9 that, for any studied electrocatalyst, as the voltage supplied to the electrocatalyst/KOH interface is made more cathodic (where H_2 gas is created excessively), the TOF value increases, resulting in improved HER kinetics.

The value of TOF increases at any applied voltage in the case of FA-TiO_2, especially at high negative values. When the evaluated electrocatalysts are exposed to cathodic activation, they exhibit a significant rise in TOF. These results provide further evidence that HER is effectively catalyzed upon hybridization of FA and TiO_2, followed by a cathodic pre-polarization process applied to the FA-TiO_2)/KOH interface.

The Faradaic efficiency (*FE*%) values of the studied electrocatalysts before and after cathodic activation for the HER were also computed in order to better examine and compare their HER electrocatalytic activity. The detailed calculations of such measurements are discussed in Section S2.3 (Supporting Information). Table 4 summarizes the data generated, namely the estimated and measured amounts of H_2 produced by the electrolysis technique employed in this study. It is noticed in Table 4 that the *FE*% value of the FA-TiO_2 nanocomposite rises and increases further after it is exposed to the cathodic polarization pre-treatment. These findings highlight again the obvious catalytic role of both the incorporated nanomaterial, namely TiO_2 and the process of cathodic activation in enhancing the kinetics of the HER on the FA-TiO_2 electrocatalyst.

Table 4. Mean value (standard deviation) of V_{H2} (measured and calculated) obtained after 1 h of a controlled galvanostatic electrolysis (CGE) *, together with the Faradaic Efficiency (FE) values, ε(%), for the studied catalysts.

Tested Electrocatalysts	Calculated H_2 Based on the Charge Passed during Electrolysis		H_2 Measured by GC (H_2/μmol h^{-1})	*FE*(%)
	Charge Passed/C	H_2/μmol h^{-1}		
GC-FA (unactivated)	2.4(0.03)	12.44	6.02(0.08)	48.4(0.6)
GC-FA (activated)	3.2(0.04)	16.58	11.24(0.15)	67.8(0.7)
GC-TiO_2 (unactivated)	3.4(0.05)	17.62	13.46(0.22)	76.4(0.9)
GC-TiO_2 (activated)	4.7(0.06)	24.36	21.66(0.36)	88.9(1.1)
GC-(FA-TiO_2) (unactivated)	4.9(0.07)	25.40	23.55(0.32)	92.7(1.3)
GC-(FA-TiO_2) (activated)	6.1(0.08)	31.61	31.17(0.42)	98.6(1.5)

* 72 h of chronopotentiometry (cathodic potential vs. time) test performed at a cathodic current density of −200 mA cm^{-2}.

3.3. Long-Term Stability Test and Origin of Catalytic Activity

The long-term stability test of the as-prepared catalyst is essential to assess its durability, one of the most substantial criteria for a viable electrocatalyst. Continuous potential cycling (up to 10,000 cycles) and chronopotentiometry (potential vs. time at a fixed cathodic current density) techniques were applied to the (FA-TiO_2)/GC catalyst to evaluate its durability, Figure 10.

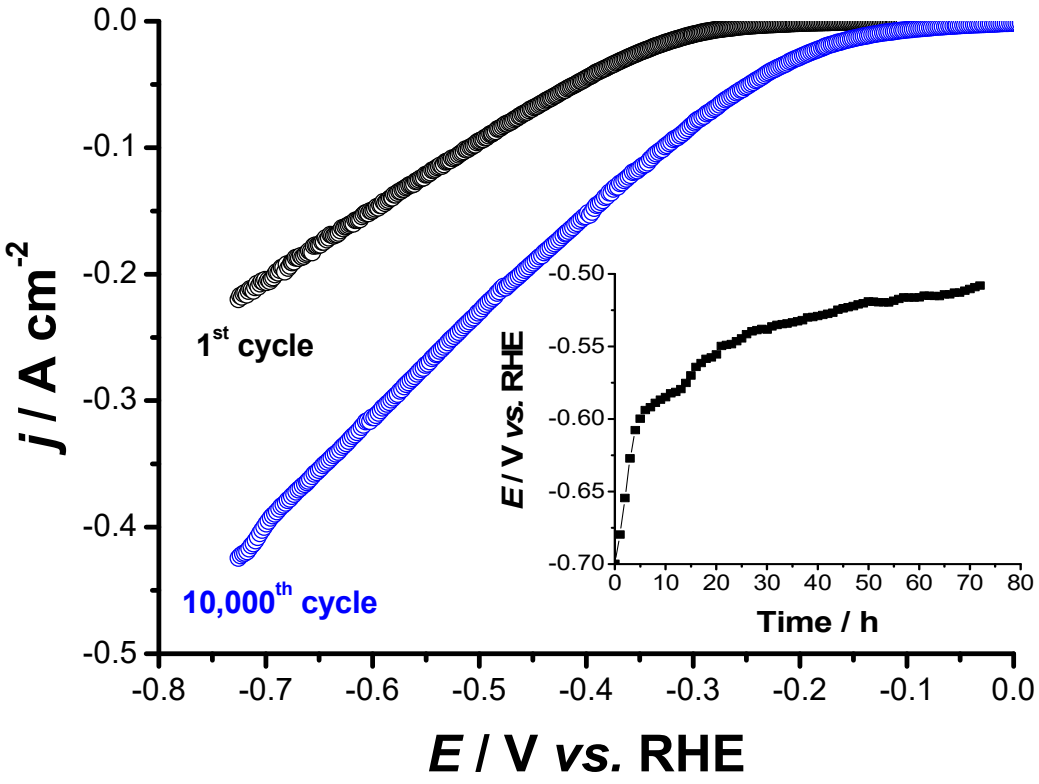

Figure 10. GC-(FA-TiO_2) catalyst's stability tests: effect of repetitive cycling (10,000 cycles)—inset: 72 h of chronopotentiometry (cathodic potential vs. time) test performed at a cathodic current density of −200 mA cm^{-2}. All measurements were conducted in deaerated 0.1 M KOH aqueous solutions at 25 °C.

After 10,000 CV cycles, the catalyst's polarization curves exhibit major shifts towards higher cathodic currents. This increase in current upon potential cycling confirms the current augmentation that has occurred during the chronoamperometry measurements (revisit Figure 7) and subsequent activation of the catalyst. This activation is boosted upon increasing the applied cathodic potential since hydrogen is profusely evolving at higher cathodic potentials. The same conclusion was drawn by electrolysis carried out at a fixed cathodic current density of -200 mA cm^{-2}, see the inset of Figure 10. The cathodic potential was markedly shifted towards the less negative values (active direction) during the operation. These results show that the GC-(FA-TiO_2) catalyst has good long-term stability and is also activated during the process.

Since the catalyst is activated during the long-term stability test, where hydrogen releases abundantly, hydrogen is expected to be incorporated into the catalyst's structure, leading to catalyst disintegration [48]. This, in turn, increases the surface roughness of the catalyst, allowing new HER catalytically active defect sites to be generated. The incorporation of hydrogen in the catalyst's crystal structure and subsequent increase in the catalyst surface roughness is translated into a pronounced increase in the catalyst's active surface area, as evidenced from CV measurements, Figure 9.

3.4. The Surface Morphology and Composition of FA-TiO_2 after Cathodic Activation

Figure 11 displays the SEM images and the corresponding EDX spectrum of FA-TiO_2 electrocatalyst after cathodic activation. As can be seen, no change was observed in terms of chemical composition after the cathodic activation process. On the other hand, the size of the activated FA-TiO_2 cenosphere decreased as compared to the inactivated FA-TiO_2 nanomaterials (10 to 100 μm before activation and 5 to 75 μm after activation). Likewise, the average particle size of the FA-TiO_2 catalyst decreased (from 10 to 15 nm before activation and 7 to 11 nm after activation) after the cathodic activation, as indicated in Figure 12. Indeed, the decrease in particle size involves, without a doubt, an increase in the specific surface area of the activated catalyst, evidenced by CV measurements, which are in good agreement with the electrochemical measurements. On the other side, we can observe that a part of the microstructure of the activated FA-TiO_2 catalyst is distorted, and many cavities were formed. This can be attributed most probably to the electrochemical attack triggered by the H_2 molecules during the cathodic activation process. Moreover, the formation of this genre of cavities can serve as additional catalytic active sites, and therefore, enhance the H_2 production process.

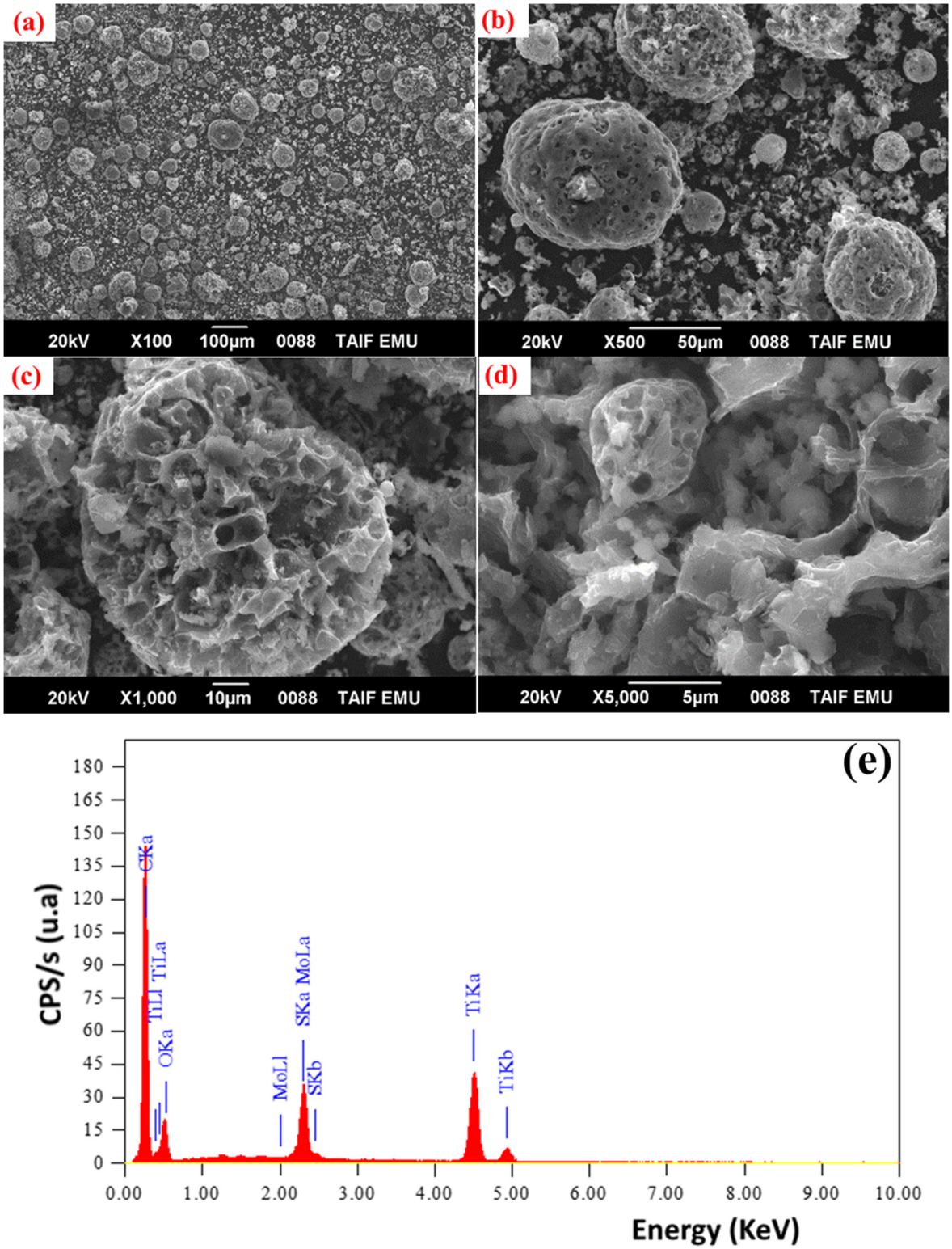

Figure 11. SEM images at different magnifications (**a**–**d**) and EDX spectrum (**e**) of the FA-TiO_2 catalyst after cathodic activation.

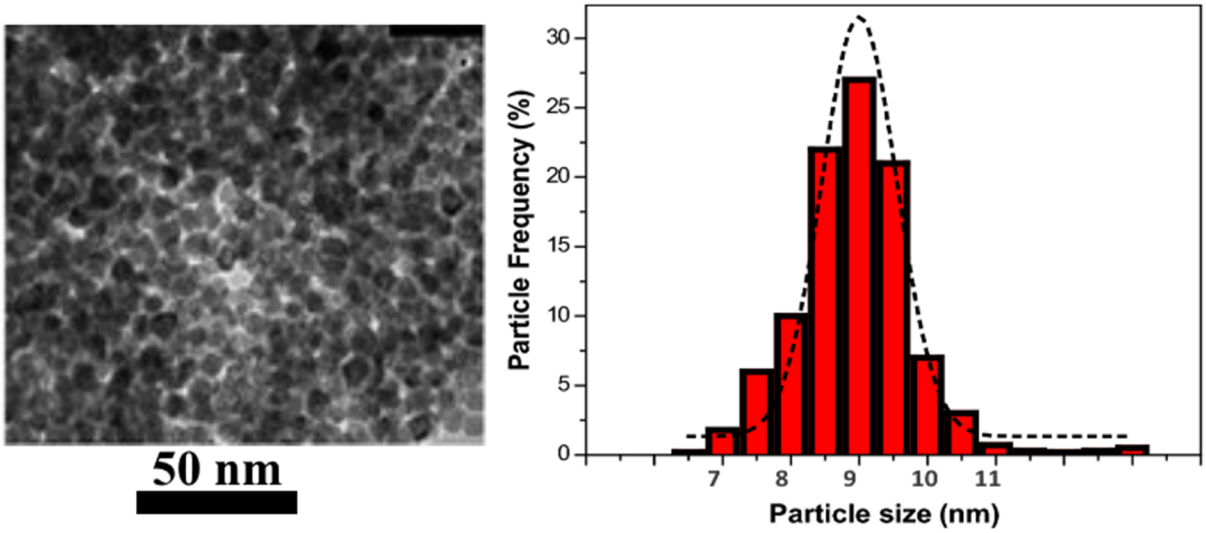

Figure 12. TEM image and size distribution histogram of the activated FA-TiO_2 catalyst.

4. Conclusions

In this work, we have successfully immobilized TiO_2 nanoparticles on fly ash FA waste by adopting the solvothermal method. The obtained FA-TiO_2 material was then fully characterized using various chemical and physical instruments and techniques. The designed FA-TiO_2 hybrid nanomaterial exhibited high thermal stability and enhanced activity compared to bare TiO_2 nanoparticles. After that, we exploited this hybrid nanomaterial to produce hydrogen via an electrochemical process as a green solution to treat this kind of waste. The linear sweep voltammetry technique was applied to the (FA-TiO_2)/OH^- interface to evaluate its catalytic activity for the HER in 0.1 M KOH solution in the dark. Before cathodic activation, the FA-TiO_2 showed a substantial catalytic performance for the HER. The unactivated FA-TiO_2 electrocatalyst recorded an onset potential (E_{HER}) value of −144 mV vs. RHE, a Tafel slope ($-b_c$) value of 124 mV dec^{-1}, and an exchange current density (j_o) of ~0.07 mA cm^{-2}. In addition, it required an overpotential value of 160 mV to generate a current density of 10 mA cm^{-2}.

Prolonged potential electrolysis of the unactivated (as-prepared) FA-TiO_2 electrocatalyst under severe cathodic polarization conditions (chronoamperometry measurements conducted at a high cathodic potential for 24 h) yielded an activated FA-TiO_2 electrocatalyst with significantly enhanced HER catalytic activity. The cathodically activated FA-TiO_2 exhibited the following electrochemical parameters for the HER kinetics: E_{HER} = −78 mV, $-b_c$ = 63 mV dec^{-1}, and j_o = 0.22 mA cm^{-2}. It acquired a reduced overpotential value of 105 mV to deliver a current density of 10 mA cm^{-2}. SEM/EDX examinations of the FA-TiO_2 electrocatalyst after the prolonged cathodic activation process revealed no change in terms of chemical composition. Compared to the unactivated FA-TiO_2, the size of the activated FA-TiO_2 cenospheres was smaller (10 to 100 µm before activation and 5 to 75 µm after activation). Similarly, after cathodic activation, the average particle size of the FA-TiO_2 catalyst decreased from 10–15 nm before activation to 7–11 nm after activation. These events resulted in increased specific surface area, and hence, enhanced HER kinetics of the activated catalyst, as evidenced from the CV measurements. Furthermore, as a result of the electrochemical attack triggered by the H_2 molecules during the cathodic activation process, a portion of the activated FA-TiO_2 catalyst's microstructure has been deformed, and several cavities were formed. As a result, such cavities can function as extra catalytic active sites, enhancing the H_2 generation process.

The current investigation might open up new routes toward the development of advanced materials from the FA waste generated from thermal power plants to be used as potential electrocatalysts for hydrogen evolution and other electrochemical processes. As a future point of research, for instance, our preliminary electrochemical characterizations

revealed that FA-TiO_2 decorated with Cu NPs exhibited high catalytic activity, which further enhanced upon decreasing the Cu NPs' size, towards overall water splitting and oxygen reduction reaction.

Supplementary Materials: The following supporting information can be downloaded at: https://www.mdpi.com/article/10.3390/catal12050466/s1. Section S1: Preparation of the GC-loaded Catalyst Working Electrode (WE). Section S2: Electrochemical studies. Table S1: Comparison of HER activity of our synthesized FA-TiO2 catalyst (before and after cathodic activation*) with Pt/C and some other, highly effective titania and titania-based electrocatalysts reported in the literature. References [10,11,51–62] are cited in the Supplementary Materials.

Author Contributions: Conceptualization, T.A. and M.M.I.; Data curation, A.M.; Formal analysis, A.A.G.; Investigation, M.S.R.; Methodology, A.M.S., A.M.M., P.K.B. and M.R.D.; Writing—review & editing, M.S.A., J.R., M.A.A. and R.B. All authors have read and agreed to the published version of the manuscript.

Funding: The Authors extend their appreciation to the Deputyship for Research & Innovation, Ministry of Education in Saudi Arabia for funding this research work through the project number 1-441-125.

Acknowledgments: The authors extend their appreciation to the Deputy for Research & Innovation, Minister of Education in Saudi Arabia for Funding this research work through the project number 125-441-1.

Conflicts of Interest: The authors declare no conflict of interest.

References

1. Ghenciu, A.F. Review of fuel processing catalysts for hydrogen production in PEM fuel cell systems. *Curr. Opin. Solid State Mater. Sci.* **2002**, *6*, 389–399. [CrossRef]
2. Kirubakaran, A.; Jain, S.; Nema, R.K. A review on fuel cell technologies and power electronic interface. *Renew. Sustain. Energy Rev.* **2009**, *13*, 2430–2440. [CrossRef]
3. Turner, J.A. Sustainable hydrogen production. *Science* **2004**, *305*, 972–974. [CrossRef] [PubMed]
4. Bhavsar, S.; Najera, M.; Solunke, R.; Veser, G. Chemical looping: To combustion and beyond. *Catal. Today* **2014**, *228*, 96–105. [CrossRef]
5. Yan, W.; Hoekman, S.K. Production of CO_2-free hydrogen from methane dissociation: A review. *Environ. Prog. Sustain. Energy* **2014**, *33*, 213–219. [CrossRef]
6. Kumar, S.S.; Himabindu, V. Hydrogen production by PEM water electrolysis—A review. *Mater. Sci. Energy Technol.* **2019**, *2*, 442–454.
7. Yan, Y.; Xia, B.; Xu, Z.; Wang, X. Recent development of molybdenum sulfides as advanced electrocatalysts for hydrogen evolution reaction. *ACS Catal.* **2014**, *4*, 1693–1705. [CrossRef]
8. Faber, M.S.; Jin, S. Earth-abundant inorganic electrocatalysts and their nanostructures for energy conversion applications. *Energy Environ. Sci.* **2014**, *7*, 3519–3542. [CrossRef]
9. Do, H.H.; Nguyen, D.L.; Nguyen, X.C.; Le, T.H.; Nguyen, T.P.; Trinh, Q.T.; Ahn, S.H.; Vo, D.N.; Kim, S.Y.; Le, Q.V. Recent progress in TiO_2-based photocatalysts for hydrogen evolution reaction: A review. *Arab. J. Chem.* **2020**, *13*, 3653–3671. [CrossRef]
10. Feng, H.; Xu, Z.; Ren, L.; Liu, C.; Zhuang, J.; Hu, Z.; Xu, X.; Chen, J.; Wang, J.; Hao, W.; et al. Activating Titania for Efficient Electrocatalysis by Vacancy Engineering. *ACS Catal.* **2018**, *8*, 4288–4293. [CrossRef]
11. Swaminathan, J.; Subbiah, R.; Singaram, V. Defect-Rich Metallic Titania ($TiO_{1.23}$)—An Efficient Hydrogen Evolution Catalyst for Electrochemical Water Splitting. *ACS Catal.* **2016**, *6*, 2222–2229. [CrossRef]
12. Prosini, P.P.; Pozio, A.; Botti, S.; Ciardi, R. Electrochemical studies of hydrogen evolution, storage and oxidation on carbon nanotube electrodes. *J. Power Sources* **2003**, *118*, 265–269. [CrossRef]
13. Cui, W.; Liu, Q.; Cheng, N.; Asiri, A.M.; Sun, X. Activated carbon nanotubes: A highly-active metal-free electrocatalyst for hydrogen evolution reaction. *Chem. Commun.* **2014**, *50*, 9340–9342. [CrossRef] [PubMed]
14. Wei, L.; Karahan, H.E.; Goh, K.; Jiang, W.; Yu, D.; Chen, Y. A high-performance metal-free hydrogen-evolution reaction electrocatalyst from bacterium derived carbon. *J. Mater. Chem. A* **2015**, *3*, 7210–7214. [CrossRef]
15. Darabdhara, G.; Amin, M.A.; Mersal, G.A.; Ahmed, E.M.; Das, M.R.; Zakaria, M.B.; Malgras, V.; Alshehri, S.M.; Yamauchi, Y.; Szunerits, S.; et al. Reduced graphene oxide nanosheets decorated with Au, Pd and Au–Pd bimetallic nanoparticles as highly efficient catalysts for electrochemical hydrogen generation. *J. Mater. Chem. A* **2015**, *3*, 20254–20266. [CrossRef]
16. Amin, M.; Fadlallah, S.A.; Alosaimi, G.S.; Kandemirli, F.; Saracoglu, M.; Szunerits, S.; Boukherroub, R. Cathodic Activation of Titanium-Supported Gold Nanoparticles: An Efficient and Stable Electrocatalyst for the Hydrogen Evolution Reaction. *Int. J. Hydrogen Energy* **2016**, *41*, 6326–6341. [CrossRef]

17. Darabdhara, G.; Das, M.R.; Amin, M.A.; Mersal, G.A.; Mostafa, N.Y.; El-Rehim, S.S.; Szunerits, S.; Boukherroub, R. Au-Ni Alloy Nanoparticles Supported on Reduced Graphene Oxide as Highly Efficient Electrocatalysts for Hydrogen Evolution and Oxygen Reduction Reactions. *Int. J. Hydrogen Energy* **2018**, *43*, 1424–1438. [CrossRef]
18. Mezni, A.; Ibrahim, M.M.; El-Kemary, M.; Shaltout, A.A.; Mostafa, N.Y.; Ryl, J.; Kumiera, T.; Altalhi, T.; Amin, M.A. Cathodically activated Au/TiO_2 Nanocomposite Synthesized by a New Facile Solvothermal Method: An Efficient Electrocatalyst With Pt-like Activity for Hydrogen Generation. *Electrochim. Acta* **2018**, *290*, 404. [CrossRef]
19. Mostafa, N.Y.; Qhtani, M.M.; Alotaibi, S.H.; Zaki, S.; Alharthi, Z.I.; Cieslik, M.; Gornicka, K.; Ryl, J.; Boukherroub, R.; Amin, M.A. Cathodic Activation of Synthesized Highly Defective Monoclinic Hydroxyl-Functionalized ZrO_2 Nanoparticles for Efficient Electrochemical Production of Hydrogen in Alkaline Media. *Int. J. Energy Res.* **2020**, *44*, 10695–10709. [CrossRef]
20. Ifires, M.; Addad, A.; Barras, A.; Hadjersi, T.; Chegroune, R.; Szunerits, S.; Boukherroub, R.; Amin, M.A. Cathodic pre-polarization studies on the carbon felt/KOH interface: An efficient metal-free electrocatalyst for hydrogen generation. *Electrochim. Acta* **2021**, *375*, 137981. [CrossRef]
21. Visa, M.; Duta, A. TiO_2/fly Ash Novel Substrate for Simultaneous Removal of Heavy Metals and Surfactants. *Chem. Eng. J.* **2013**, *223*, 860–868. [CrossRef]
22. Lu, Z.; Zhou, W.; Huo, P.; Luo, Y.; He, M.; Pan, J.; Li, C.; Yan, Y. Performance of a Novel TiO_2 Photocatalyst Based on the Magnetic Floating Fly-ash Cenospheres for the Purpose of Treating Waste by Waste. *Chem. Eng. J.* **2013**, *225*, 34–42. [CrossRef]
23. Visa, M.; Andronic, L.; Duta, A. Fly ash-TiO_2 Nanocomposite Material for Multi-pollutants Wastewater Treatment. *J. Environ. Manag.* **2015**, *150*, 336–343. [CrossRef] [PubMed]
24. Visa, M.; Isac, L.; Duta, A. New fly ash TiO_2 Composite for the Sustainable Treatment of Wastewater with Complex Pollutants Load Maria. *Appl. Surf. Sci.* **2015**, *339*, 62–68. [CrossRef]
25. Saud, P.S.; Pant, B.; Park, M.; Chae, S.; Park, S.J.; EI-Newehy, M.; Al-Deyab, S.S.; Kim, H.Y. Preparation and Photocatalytic Activity of Fly ash Incorporated TiO_2 Nanofibers for Effective Removal of Organic Pollutants. *Ceram. Int.* **2015**, *41*, 1771–1777. [CrossRef]
26. Sharma, R.; Shaw, R.; Tiwari, S.; Tiwar, S. Nano-Titania Decorated Fly Ash as Self-Cleaning Antibacterial Cool Pigment. *ACS Sustain. Chem. Eng.* **2015**, *11*, 2796–2803. [CrossRef]
27. Yang, L.; Wang, F.; Hakki, A.; Macphee, D.E.; Hu, P. The Influence of Zeolites Fly Ash bead/TiO_2 Composite Material Surface Morphologies on their Adsorption and Photocatalytic Performance. *Appl. Surf. Sci.* **2017**, *392*, 687–696. [CrossRef]
28. Kanakaraju, D.; Hazimbin, M.; Lim, Y.C.; Pace, A. Combined Adsorption/Photocatalytic Dye Removal by Copper-Titania-fly Ash Composite. *Surf. Interfaces* **2020**, *19*, 100534. [CrossRef]
29. Chen, J.-W.; Yuan, B.; Shi, J.-W.; Yang, J.-C.; Fu, M.L. Reduced Graphene Oxide and Titania Nanosheet Cowrapped Coal Fly ash Microspheres Alternately as a Novel Photocatalyst for Water Treatment. *Catal. Today* **2018**, *315*, 247–254. [CrossRef]
30. Donga, Y.; Hampshirea, S.; Zhoub, J.; Lin, B.; Jia, J.; Meng, M. Recycling of Fly Ash for Preparing Porous Mullite Membrane Supports With Titania Addition. *J. Hazard. Mater.* **2010**, *180*, 173–180. [CrossRef]
31. Mushtaqa, F.; Zahid, M.; Bhatti, I.A.; Nasir, S.; Hussain, T. Possible Applications of Coal Fly Ash in Wastewater Treatment. *J. Environ. Manag.* **2019**, *240*, 27–46. [CrossRef] [PubMed]
32. Zhang, L.; Tu, L.; Liang, Y.; Chen, Q.; Li, Z.; Li, C.; Li, W. Coconut-Based Activated Carbon Fibers for Efficient Adsorption of Various Organic Dyes. *RSC Adv.* **2018**, *8*, 42280–42291. [CrossRef]
33. Sankaran, K.; Ficek, M.; Panda, K.; Yeh, C.J.; Sawczak, M.; Ryl, J.; Leou, K.C.; Park, J.Y.; Lin, I.N.; Bogdanowicz, R.; et al. Boron-Doped Nanocrystalline Diamond–Carbon Nanospike Hybrid Electron Emission Source. *ACS Appl. Mater. Interfaces* **2019**, *11*, 48612–48623. [CrossRef] [PubMed]
34. Park, H.; Lee, S.H.; Kim, F.S.; Choi, H.H.; Cheong, I.W.; Kim, J.H. Enhanced Thermoelectric Properties of PEDOT:PSS Nanofilms by a Chemical Dedoping Process. *J. Mater. Chem. A* **2014**, *2*, 6532–6539. [CrossRef]
35. Sobaszek, M.; Siuzdak, K.; Sawczak, M.; Ryl, J.; Bogdanowicz, R. Fabrication and Characterization of Composite TiO_2 Nanotubes/boron-doped Diamond Electrodes Towards Enhanced Supercapacitors. *Thin Solid Films* **2016**, *601*, 35–40. [CrossRef]
36. Fu, B.; Hower, J.C.; Dai, S.; Mardon, S.M.; Liu, G. Determination of Chemical Speciation of Arsenic and Selenium in High-As Coal Combustion Ash by X-ray Photoelectron Spectroscopy: Examples from a Kentucky Stoker Ash. *ACS Omega* **2018**, *3*, 17637–17645. [CrossRef]
37. Wu, H.; Zhu, Y.; Bian, S.; Ko, J.H.; Li, S.Y.; Xu, Q. H_2S Adsorption by Municipal Solid Waste Incineration (MSWI) Fly Ash with Heavy Metals Immobilization. *Chemosphere* **2018**, *195*, 40–47. [CrossRef]
38. Li, D.; Jing, P.; Sun, L.; An, Y.; Shan, X.; Lu, X.; Zhou, D.; Han, D.; Shen, D.; Zhai, Y.; et al. Near-Infrared Excitation/Emission and Multiphoton-Induced Fluorescence of Carbon Dots. *Adv. Mater.* **2018**, *30*, 1705913. [CrossRef]
39. Grochowska, K.; Molenda, Z.; Karczewski, J.; Bachmann, J.; Darowicki, K.; Ryl, J.; Siuzdak, K. Laser Induced Formation of Copper Species over TiO_2 Nanotubes Towards Enhanced Water Splitting Performance. *Int. J. Hydrogen Energy* **2020**, *45*, 19192–19205. [CrossRef]
40. Dubouis, N.; Grimaud, A. The Hydrogen Evolution Reaction: From Material to Interfacial Descriptors. *Chem. Sci.* **2019**, *10*, 9165–9181. [CrossRef]
41. Vilekar, S.A.; Fishtik, I.; Dattaz, R. Kinetics of the Hydrogen Electrode Reaction. *J. Electrochem. Soc.* **2010**, *157*, 1040–1050. [CrossRef]
42. Conway, B.E.; Tilak, B.V. Interfacial Processes Involving Electrocatalytic Evolution and Oxidation of H_2, and the Role of Chemisorbed H. *Electrochim. Acta* **2002**, *47*, 3571–3594. [CrossRef]

43. Skulason, E.; Tripkovic, V.; Bjorketun, M.E.; Gudmundsdottir, S.; Karlberg, G.; Rossmeisl, J.; Bligaard, T.; Jonsson, H.; Nørskov, J.K. Modeling the Electrochemical Hydrogen Oxidation and Evolution Reactions on the Basis of Density Functional Theory Calculations. *J. Phys. Chem. C* **2010**, *11*, 18182–18197. [CrossRef]
44. Nolan, H.; McEvoy, N.; O'Brien, M.; Berner, N.C.; Im, C.; Hallam, T.; McDonald, A.R.; Duesberg, G.S. Molybdenum Disulfide/pyrolytic Carbon Hybrid Electrodes for Scalable Hydrogen Evolution. *Nanoscale* **2014**, *6*, 8185–8191. [CrossRef] [PubMed]
45. Chen, W.F.; Muckerman, J.T.; Fujita, E. Recent Developments in Transition Metal Carbides and Nitrides as Hydrogen Evolution Electrocatalysts. *Chem. Commun.* **2013**, *49*, 8896–8909. [CrossRef]
46. Benck, J.D.; Hellstern, T.R.; Kibsgaard, J.; Chakthranont, P.; Jaramillo, T.F. Catalyzing the Hydrogen Evolution Reaction (HER) with Molybdenum Sulfide Nanomaterials. *ACS Catal.* **2014**, *4*, 3957–3971. [CrossRef]
47. Liu, N.; Guo, Y.; Yang, X.; Lin, H.; Yang, L.; Shi, Z.; Zhong, Z.; Wang, S.; Tang, Y.; Gao, Q. Microwave-Assisted Reactant-Protecting Strategy toward Efficient MoS_2 Electrocatalysts in Hydrogen Evolution Reaction. *ACS Appl. Mater. Interfaces* **2015**, *7*, 23741–23749. [CrossRef]
48. Xie, J.; Zhang, J.; Li, S.; Grote, F.; Zhang, X.; Zhang, H.; Wang, R.; Lei, Y.; Pan, B.; Xie, Y. Controllable Disorder Engineering in Oxygen-Incorporated MoS_2 Ultrathin Nanosheets for Efficient Hydrogen Evolution. *J. Am. Chem. Soc.* **2013**, *135*, 17881–17888. [CrossRef]
49. Tang, T.; Jiang, W.J.; Niu, S.; Liu, N.; Luo, H.; Chen, Y.Y.; Jin, S.F.; Gao, F.; Wan, L.J.; Hu, J.S. Electronic and Morphological Dual Modulation of Cobalt Carbonate Hydroxides by Mn Doping toward Highly Efficient and Stable Bifunctional Electrocatalysts for Overall Water Splitting. *J. Am. Chem. Soc.* **2017**, *139*, 8320–8328. [CrossRef]
50. Kibsgaard, J.; Jaramillo, T.F. Molybdenum Phosphosulfide: An Active, Acid-Stable, Earth-Abundant Catalyst for the Hydrogen Evolution Reaction. *Angew. Chem. Int. Ed.* **2014**, *53*, 14433–14437. [CrossRef]
51. Cha, H.G.; Song, J.; Kim, H.S.; Shin, W.; Yoon, K.B.; Kang, Y.S. Facile Preparation of Fe_2O_3 Thin Film with Photoelectrochemical Properties. *Chem. Commun.* **2011**, *47*, 2441–2443. [CrossRef] [PubMed]
52. Cao, Y.; Wu, Y.; Badie, C.; Cadot, S.; Camp, C.; Quadrelli, E.A.; Bachmann, J. Electrocatalytic Performance of Titania Nanotube Arrays Coated with MoS_2 by ALD toward the Hydrogen Evolution Reaction. *ACS Omega* **2019**, *4*, 8816–8823. [CrossRef] [PubMed]
53. Danilov, F.I.; Tsurkan, A.; Vasil'Eva, E.; Protsenko, V. Electrocatalytic activity of composite Fe/TiO_2 electrodeposits for hydrogen evolution reaction in alkaline solutions. *Int. J. Hydrog. Energy* **2016**, *41*, 7363–7372. [CrossRef]
54. Singh, K.P.; Shin, C.H.; Lee, H.Y.; Razmjooei, F.; Sinhamahapatra, A.; Kang, J.; Yu, J.S. TiO_2/ZrO_2 Nanoparticle Composites for Electrochemical Hydrogen Evolution. *ACS Appl. Nano Mater.* **2020**, *3*, 3634–3645. [CrossRef]
55. Tahira, A.; Ibupoto, Z.H.; Mazzaro, R.; You, S.; Morandi, V.; Natile, M.M.; Vagin, M.; Vomiero, A. Advanced Electrocatalysts for Hydrogen Evolution Reaction Based on Core-Shell MoS2/TiO2 Nanostructures in Acidic and Alkaline Media. *ACS Appl. Energy Mater.* **2019**, *2*, 2053–2062. [CrossRef]
56. Yu, J.; Zhou, W.; Xiong, T.; Wang, A.; Chen, S.; Chu, B. Enhanced Electrocatalytic Activity of Co@N-doped Carbon Nanotubes by Ultra Small Defect-rich TiO_2 Nanoparticles for Hydrogen Evolution Reaction. *Nano Res.* **2017**, *10*, 2599–2609. [CrossRef]
57. Yuan, M.; Zhu, Y.; Deng, L.; Ming, R.; Zhang, A.; Li, W.; Chai, B.; Ren, Z. IrO_2-TiO_2 Electrocatalyst for the Hydrogen Evolution Reaction in Acidic Water Electrolysis Without Activation. *New J. Chem.* **2017**, *41*, 6152–6159. [CrossRef]
58. Kumar, M.P.; Murugadoss, G.; Mangalaraja, R.V.; Arunachalam, P.; Kumar, M.R.; Hartley, U.W.; Salla, S.; Rajabathar, J.; ALOthman, Z.A.; ALTalhi, T. Design and Development of Defect Rich Titania Nanostructure for Efficient Electrocatalyst for Hydrogen Evolution Reaction in an Acidic Electrolyte. *J. Mater. Res. Technol.* **2021**, *14*, 2739–2750. [CrossRef]
59. Rüdiger, C.; Maglia, F.; Leonardi, S.; Sachsenhauser, M.; Sharp, I.D.; Paschos, O.; Kunze, J. Surface Analytical Study of Carbothermally Reduced Titania Films for Electrocatalysis Application. *Electrochim. Acta* **2012**, *71*, 1–9. [CrossRef]
60. Ren, B.; Jin, Q.; Li, Y.; Li, Y.; Cui, H.; Wang, C. Activating Titanium Dioxide as a New Efficient Electrocatalyst: From Theory to Experiment. *ACS Appl. Mater. Interfaces* **2020**, *12*, 11607–11615. [CrossRef]
61. Ibrahim, M.M.; Mezni, A.; Alsawat, M.; Kumeria, T.; Das, M.R.; Alzahly, S.; Aldalbahi, A.; Gornicka, K.; Ryl, J.; Amin, M.A.; et al. Enhanced Hydrogen Evolution Reaction on Highly Stable Titania-Supported PdO and Eu2O3 Nanocomposites in a Strong Alkaline Solution. *Int. J. Energy Res.* **2019**, *43*, 5367–5383. [CrossRef]
62. Ibrahim, M.M.; Mezni, A.; Alsawat, M.; Kumeria, T.; Alrooqi, A.; Shaltout, M.R.; Ahmed, S.I.; Boukherroub, R.; Amin, M.A.; Altalhi, T. Crystalline ZnO and ZnO/TiO_2 Nanoparticles Derived from Tert-butyl N-(2 mercaptoethyl)carbamatozinc(II) Chelate: Electrocatalytic Studies for H2 Generation in Alkaline Electrolytes. *Int. J. Energy Res.* **2020**, *44*, 6725–6744. [CrossRef]